Journal of Zhejiang University-SCIENCE A (Applied Physics & Engineering) *2024 25(9):716-731*
www.jzus.zju.edu.cn; www.springer.com/journal/11582
E-mail: jzus_a@zju.edu.cn

Research Article
https://doi.org/10.1631/jzus.A2300307

Effect of geometry simplification and boundary condition specification on flow field and aerodynamic noise in the train head and bogie region of high-speed trains

Jiawei SHI[1]✉, Yuan HE[2], Jiye ZHANG[1], Tian LI[1]

[1]*State Key Laboratory of Rail Transit Vehicle System, Southwest Jiaotong University, Chengdu 610031, China*
[2]*Institute of Sound and Vibration Research, Faculty of Engineering and Physical Sciences, University of Southampton, Southampton SO17 1BJ, UK*

Abstract: The purpose of this study is to determine a suitable modeling method to make computational fluid dynamics (CFD) simulation more efficient for aeroacoustics optimization of the bogie region of high-speed trains. To this end, four modeling methods are considered, which involve different geometry simplifications and boundary condition specifications. The corresponding models are named the three-car marshalling model, computational domain shortening model, carbody shortening model, and sub-domain model. Combining the detached eddy simulation (DES) model and Ffowcs Williams-Hawkings (FW-H) equation, the unsteady flow field and far-field noise of the four models are predicted. To evaluate the effect of the different modeling methods, the time-averaged flow field, fluctuating flow field, and far-field noise results of the four models are compared and analyzed in detail with the results of the three-car marshalling model used as basis for comparison. The results show that the flow field results of the bogie region predicted by the four models have relatively high consistency. However, the usage of the non-time varying outlet boundary conditions in the computational domain shortening model and sub-domain model could affect the pressure fluctuation on the upstream carbody surface. When only the bogie region is used as the source surface, the differences between the far-field noise results of the three simplified models and the three-car marshalling model are all within 1 dB; when the train head is used as the source surface, the results of the carbody shortening model and the three-car marshalling model are more consistent.

Key words: Bogie region; Train head; Flow field; Aerodynamic noise; Geometry simplification; Boundary conditions

1 Introduction

With the continuous improvements in train operation speed, the problems related to train aerodynamics are increasingly prominent, one of which is aerodynamic noise (Thompson, 2008; Meskine et al., 2013; Thompson et al., 2015). As with other aerodynamic problems, optimization of train aeroacoustics performance mainly relies on wind tunnel test and numerical simulation. The length of a typical eight-car high-speed train is about 200 m. Such a large size makes it impossible to conduct wind tunnel tests on full-scale train models. In China, the 1:8 scale three-car model is commonly used for wind tunnel tests (Ding et al., 2016; Li et al., 2022). Research on Reynolds number effects and observation of the flow field in the middle of the train have demonstrated the rationality of this approach (Khier et al., 2000; Bell et al., 2017; Chang et al., 2022). The biggest advantage of the wind tunnel test is its high reliability, but it is not suitable for large-scale shape parameter optimization, because it is usually difficult to implement shape modification on a physical prototype used for wind tunnel test. With the rapid development of computational technologies, numerical simulation has become another option for aerodynamic and aeroacoustics optimization. Compared with the wind tunnel test, the model configuration is more flexible in numerical simulation, and a large number of design modifications can be completed in a short period of time. However, in terms of aerodynamic noise, it is still a time-consuming work

✉ Jiawei SHI, sjw7001@126.com
Jiawei SHI, https://orcid.org/0009-0007-8850-9926

Received June 8, 2023; Revision accepted Nov. 27, 2023;
Crosschecked June 23, 2024; Online first Aug. 3, 2024

to predict the response to design changes through numerical simulation due to the high requirements of grid size, time step size, and geometry accuracy.

In aerodynamic drag optimization, the influence of changes in component shape must be evaluated on a whole vehicle model. However, the main noise sources of high-speed trains are relatively independent and there is not a strong coupling effect among the flow field and sound field of different sources. Therefore, when optimizing train aeroacoustics performance, the components as the main noise sources can be optimized one by one (Li et al., 2020b). The bogie region is one of the most important aerodynamic noise sources of high-speed trains (Thompson, 2008; Lauterbach et al., 2012; Meskine et al., 2013; Thompson et al., 2015; Li et al., 2022). Numerous experimental and numerical results have shown that although a high-speed train has multiple bogies, the aerodynamic noise generated by the first bogie of the leading car is far greater than that generated by other bogies (Thompson, 2008; Meskine et al., 2013; Thompson et al., 2015; Li et al., 2022). Therefore, aerodynamic noise control of the bogie region should be focused on the first bogie of the leading car. In view of this, the three-car model seems not to be the most suitable choice for computational fluid dynamics (CFD)-based aeroacoustics optimization of the bogie region, because the areas we are really interested in are only concentrated at the train head and the foremost bogie region, while the use of a three-car model makes a large number of grids wasted in areas that have little impact on the flow phenomenon of interest. To make CFD simulation more efficient for aeroacoustics optimization of the bogie region, a suitable modeling method is needed.

In fact, due to the high computational cost of aeroacoustics simulation, many studies on aerodynamic noise have attempted to use some model simplification methods to improve the efficiency of CFD simulation. In a study on aerodynamic noise generated by the head streamlined surface of a high-speed train (Liu et al., 2011), the streamlined surfaces of the head car and tail car were directly connected to build a geometry model. The authors evaluated the effect of the middle body length on pressure distribution on the carbody surface by steady Reynolds-averaged Navier-Stokes (RANS) simulation and found that when the middle length is greater than 8 m, further increase in the middle body length has little effect on the pressure distribution on the carbody surface. However, it is not clear how the middle body length affects the aerodynamic noise of the head streamlined surface. Minelli et al. (2020) used a computational domain shortening model to study the aerodynamic noise generated by a simplified Inter City Express (ICE) train head. In their model, the train geometry was truncated by the outlet of the computational domain at the middle of the head car and the outlet boundary was set as pressure outlet with gauge pressure of 0. In a study on wind noise generated by the A-pillar and side mirror region of a heavy truck (Yao et al., 2018), the researchers tried to reduce the simulation cost by simplifying the trailer model, including removing some components from the trailer and modifying the tail shape. The simulation results show that these simplifications have little effect on flow characteristics in the A-pillar region. This also indicates that the geometrical modification of downstream components has a limited effect on the flow field around the distant upstream components. The sub-domain model is also a method to enhance the computational efficiency of aerodynamic noise simulation. The so-called sub-domain is a part of a larger computational domain. During the simulation, the time-averaged flow field of the large computational domain is first calculated by steady RANS simulation, and the obtained flow field data are mapped to the boundary of the sub-domain as boundary conditions for further analysis through unsteady simulation. Karbon and Dietschi (2005) applied the sub-domain method to the aeroacoustics optimization of a passenger car's roof rack. The dominant frequency and ranking of the sound pressure level of different models predicted by CFD simulation are in good agreement with the wind tunnel test results. In a recent study, Schell and Eiselt (2020) employed the sub-domain method to simulate the squealing of a car side mirror. Their simulation reproduced this complex aeroacoustic feedback phenomenon and accurately captured the frequency associated with the squealing. In recent years, the sub-domain method has also been applied to the aerodynamic noise simulation of high-speed trains. Gao et al. (2017) tried to predict the aerodynamic noise of a full-scale train head shape with the sub-domain method. Zhao et al. (2020) validated the effectiveness of the sub-domain method based on a 1:40 scale train model, and observed that the numerical results of the time-averaged vorticity distribution in the wake of the pantograph

closely resembled those obtained by the particle image velocimetry (PIV) test. Furthermore, they found that the pressure-spectrum structures of the two measurement points on the carbody surface obtained by the simulation are consistent with the test results, albeit with an overall pressure level difference of about 3.8 dB.

Based on the above review, it is evident that various modeling methods have been applied for aerodynamic noise simulation of the bogie region or could serve as a reference for this. However, there is currently a lack of research that quantitatively compares the flow field and aerodynamic noise obtained from different modeling methods. In this study, four modeling methods applied to the aerodynamic noise simulation of the bogie region are considered, which involve different geometry model simplifications and boundary condition specifications. The four models are called the three-car marshalling model, the computational domain shortening model, the carbody shortening model, and the sub-domain model. In a sense, the last three models can be regarded as simplified versions of the three-car marshalling model. A comparative analysis is conducted on the simulation results of the four models, with the results of the three-car marshalling model used as basis for comparison, to evaluate the effectiveness of different modeling methods in accurately reproducing the flow field and far-field noise in the train head and bogie region. The results will provide a basis for the selection of modeling methods for subsequent research on aerodynamic noise control measures for the bogie region.

2 Numerical methods

2.1 Detached eddy simulation (DES) model

DES is a hybrid method. Its basic idea is to use the large eddy simulation (LES) model in the separated zone and the RANS model in the near wall region, which offers a good compromise between accuracy and cost. Control of the solving region of the two models is achieved by modifying the length scale in the original turbulence model. Two variants of the original DES model have been proposed successively, which are the delayed detached eddy simulation (DDES) and the improved delayed detached eddy simulation (IDDES) (Spalart et al., 2006; Shur et al., 2008), and both of them are widely used to calculate the unsteady flow field around high-speed trains (Zhu and Hu, 2017; Guo et al., 2020; Li et al., 2020a; Minelli et al., 2020; Wang et al., 2020; Shi et al., 2024). In current study, the shear stress transport (SST) k-ω based DDES model is used to numerically solve the unsteady flow field in the bogie region.

2.2 Ffowcs Williams-Hawkings (FW-H) acoustic analogy

The FW-H equation, as shown in Eq. (1), is the basic equation of the aeroacoustics (Williams and Hawkings, 1969):

$$\frac{1}{c_0^2}\frac{\partial^2}{\partial t^2}\left[p'H(f)\right]-\nabla^2\left[p'H(f)\right]=\frac{\partial}{\partial t}\left[\rho_0 v_{\mathrm{n}}\delta(f)\right]-\frac{\partial}{\partial x_i}\left[p_{ij}\hat{n}_j\delta(f)\right]+\frac{\partial^2}{\partial x_i\partial x_j}\left[T_{ij}H(f)\right], \tag{1}$$

where c_0 is the speed of sound, t indicates the time, p' is the sound pressure, x_i (i=1, 2, 3) is the Cartesian coordinate component, $f=0$ is the equation of the source surface, $H(\cdot)$ is the Heaviside function, $\delta(\cdot)$ is the Dirac function, ρ_0 is the density of the undisturbed fluid, v_{n} is the component of the sound source surface velocity in the outward normal direction, $\hat{n}_j$ is the element of unit vector of the outward normal direction at a point on the source surface, $p_{ij}=p\delta_{ij}-\sigma_{ij}$ is the element of fluid compressive stress tensor, p is the pressure, δ_{ij} is the element of Kronecker tensor, σ_{ij} represents the viscous stress, ∇ is the Nabla operator, and T_{ij} is the element of Lighthill stress tensor.

According to Lighthill's acoustic analogy, the three terms at the right end of Eq. (1) correspond to the monopole source, dipole source, and quadrupole source. By using Green's function from classical acoustics, the far-field sound pressure can be expressed as the superposition of the contributions of the three source terms. In this study, the quadrupole source term is neglected due to its low radiation efficiency in low Mach number flow and minimal contribution to far-field noise. In addition, the numerical simulation is based on wind tunnel mode. The train surface remains static and rigid, so the monopole source term is also equal to 0. Consequently, the far-field noise only includes the contribution of dipole sources, which can be expressed by Eq. (2) (Farassat, 2007):

$$p'(\boldsymbol{x},\,t)=\frac{1}{4\pi c_0}\int_{f=0}\left[\frac{\dot{l}_{\mathrm{r}}}{r(1-M_{\mathrm{r}})^2}\right]_{\mathrm{ret}}\mathrm{d}S+\frac{1}{4\pi}\int_{f=0}\left[\frac{l_{\mathrm{r}}-l_{\mathrm{M}}}{r^2(1-M_{\mathrm{r}})^2}\right]_{\mathrm{ret}}\mathrm{d}S+\frac{1}{4\pi c_0}\int_{f=0}\left[\frac{l_{\mathrm{r}}\left(r\dot{M}_{\mathrm{r}}+c_0M_{\mathrm{r}}-c_0M^2\right)}{r^2(1-M_{\mathrm{r}})^3}\right]_{\mathrm{ret}}\mathrm{d}S,\tag{2}$$

$$l_{\mathrm{r}}=l_i\hat{r}_i,\quad \dot{l}_{\mathrm{r}}=\dot{l}_i\hat{r}_i,\quad l_{\mathrm{M}}=l_iM_i,\quad M_{\mathrm{r}}=M_i\hat{r}_i,$$

where $l_i=p_{ij}\hat{n}_j$, M_i is the component of the Mach number of the sound source (M) in the x_i direction, r is the distance between a point $\boldsymbol{y}$ on the source surface and receiver point $\boldsymbol{x}$, and $\hat{r}_i$ is the element of unit vector of $\boldsymbol{y}$ pointing to $\boldsymbol{x}$. The subscript 'ret' of the integral term indicates that the relevant variables are evaluated at the restarted time $\tau=t-r/c_0$.

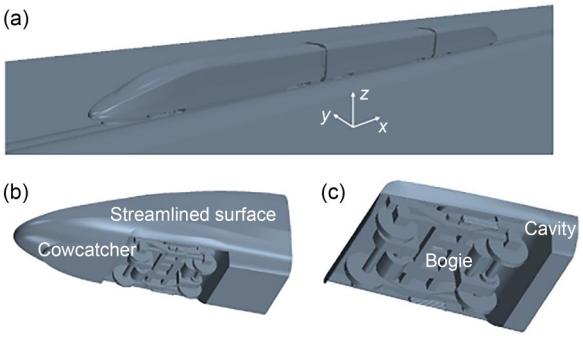

Fig. 1 Geometry model: (a) three-car marshalling model; (b) train head; (c) bogie region

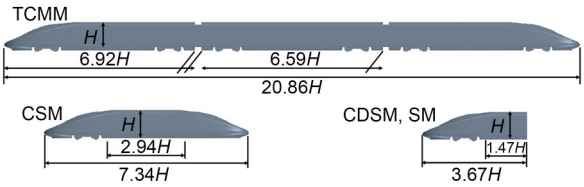

Fig. 2 Schematic diagram of train geometry and size

3 CFD model

3.1 Geometry model, computational domain, and boundary conditions

A 1:8 scale electric multiple unit (EMU) model is taken as the research object. Fig. 1a shows a three-car model consisting of a head car, mid car, and tail car. The coordinate system defined for current simulation is also depicted in Fig. 1a, with the negative direction of the x-axis aligned with the train operation direction. Figs. 1b and 1c further show the geometry of the train head and bogie region, which will be used as source surfaces for far-field noise calculation. Although simplified to some extent, the bogie model is still sufficient to reflect the structural characteristics of its real counterpart (Dong et al., 2019).

In addition to the three-car marshalling model (abbreviated as TCMM below), three simplified models are established, namely the computational domain shortening model (CDSM), carbody shortening model (CSM), and sub-domain model (SM), as shown in Fig. 2. The carbody height H=474.5 mm is taken as the characteristic length, and the relevant geometry sizes are also marked in Fig. 2. The total length of the TCMM is 20.86H. In the case of CSM, a straight smooth surface connects the streamlined surface of the head car and tail car over a length of 2.94H. The foremost bogie configuration is preserved while the rear one is removed. For the CDSM and SM, the head car is truncated by the outlet boundary, and the reserved middle body length is about 1.47H.

The computational domains established for the four models are shown in Fig. 3. For the TCMM, the distance from the inlet of the domain to the nose tip of the head car is 20.00H. The width and height of the domain are 18.20H and 10.54H, respectively, making the blocking ratio less than 0.5%, which is sufficient to simulate the operation condition of a train running in open air. The distance from the nose tip of the train tail to the outlet of the domain is 45.00H, which is sufficient to ensure full development of the wake flow of the train. For the CSM, SM, and CDSM, the width and height of the domain and the distance from the nose tip of the head car to the inlet of the domain are the same as those of the TCMM, while for the CDSM and SM, the outlet boundary truncates the carbody in the middle of the head car. For the CSM, meanwhile, the distance from the nose tip of the train tail to the outlet of the domain is slightly shorter than that of the TCMM. For all four models, the inlet boundary of the computational domain is set as velocity inlet with an inflow velocity of 69.44 m/s. The both sides and top of the domain are defined as symmetry boundary. The ground and track are defined as no-slip moving wall, whose velocity is the same as the inflow velocity. The outlet of the computational domain is defined as pressure

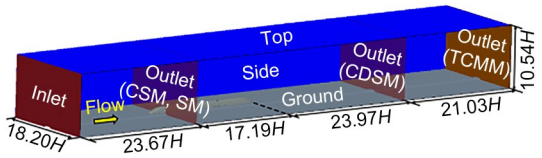

Fig. 3 Computational domain and boundary conditions

outlet. For the TCMM, CDSM, and CSM, the gauge pressure is set as 0. For the SM, the pressure and turbulence parameters at the outlet boundary are obtained by a steady RANS simulation based on the TCMM.

3.2 Mesh generation

The trimmed mesh (a kind of Hexa-dominant mesh) is used to discretize the computational domain. The maximum grid size of the head streamlined surface is 3.0 mm. The maximum surface grid size of the bogie and cavity is 1.5 mm. The blocks used for local refinements of the volume mesh in the TCMM are shown in Fig. 4a. As for the three simplified models, the same refinement strategy is used, but the size and position of the refinement blocks are adjusted according to the length of the train model. There are 15 layers of prism grids on the train surface. The initial height of the prism grids is 0.01 mm, and the stretching ratio of the prism grids is 1.2. The wall $y+$ values in most areas of the train surface are less than 1, meeting the requirements of the DES model. Fig. 4b shows the meshing results of the TCMM. Table 1 lists the volume cell counts of the four models.

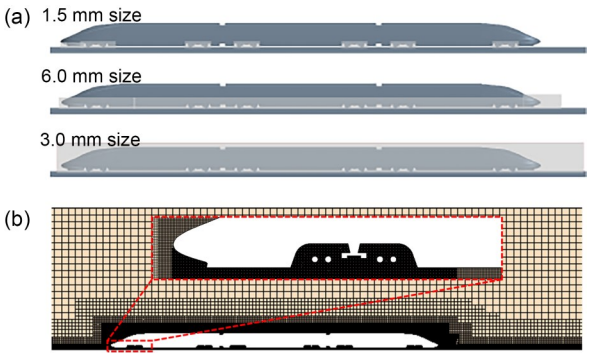

Fig. 4 Refinement blocks and meshing result (TCMM): (a) blocks for local refinements of the volume grids; (b) meshing result

3.3 Solver setting

In the simulation, the air is defined as a gas with constant density because the inflow Mach number is less than 0.3. The semi-implicit method for pressure linked equation (SIMPLE) algorithm based segregated flow solver is selected to solve the discretized flow governing equation system. The second-order implicit scheme is adopted for time discretization, and the time step is set as 5×10^{-5} s. The convective Courant-Friedrichs-Lewy (CFL) numbers of most cells in the domain are below 2.5 (check after calculation), which are enough to achieve a stable solving (Siemens PLM software, 2017). A convergent steady field obtained by RANS model is used to initialize the unsteady simulation. After the running of the first 0.4 s of the simulation that ensures the full development of the transient flow field, the flow field data are collected for another 0.25 s for far-field noise calculation. For the SM, an additional steady RANS simulation based on the TCMM is needed to obtain the boundary conditions of the sub-domain outlet. This RANS simulation lasts for 4500 steps to ensure convergence. The averaged values of pressure and turbulence parameters of the last 1000 iterations are recorded and mapped to the sub-domain outlet as boundary conditions.

Table 1 Volume cell counts of the four models

Model	Number of cells
TCMM	120 million
CDSM	25 million
CSM	33 million
SM	25 million

4 Validation of the mesh strategy and numerical methods

4.1 Clean cavity case

The flow field in the bogie region shows certain cavity flow characteristics due to the bogie cavity (Shi and Zhang, 2024). Therefore, the ‘clean cavity’ (no object in the cavity) model is selected as a case to validate the mesh strategy and numerical methods. This case is based on the experiments in (Plentovich et al., 1993). The cavity has a length-depth ratio of 6∶1 and width-depth ratio of 4∶1, which are close to the geometrical characteristics of the bogie cavity in current study. The depth and length of the cavity are d_1=61 mm and D_1=366 mm, respectively, and the Mach number of incoming flow is equal to 0.2. The

corresponding computational domain and boundary conditions are shown in Fig. 5, which are established by referring to the settings used by Kim et al. (2020).

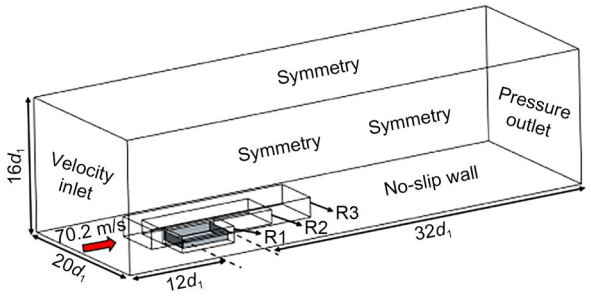

Fig. 5 Computational domain of the clean cavity case

To test the influence of grid size, three sets of meshes are established by modifying the surface grid size of the cavity and the volume grid size in blocks R1–R3 (marked in Fig. 5), named mesh1–mesh3. The number of volume cells of them are 2.8 million, 6 million, and 8 million, respectively. Detailed mesh parameters are listed in Table 2, and the mesh parameters of mesh2 correspond to the grid size of the bogie cavity surface in current study.

Table 2 Mesh parameters of the clean cavity case

Part	Grid size (mm)		
	mesh1	mesh2	mesh3
Cavity	1.8	1.5	1.2
Region1 (R1)	1.8	1.5	1.2
Region2 (R2)	3.6	3.0	2.4
Region3 (R3)	7.2	6.0	4.8

Fig. 6 presents a comparison between the pressure coefficient C_p ($C_p=(p-p_\infty)/(0.5\rho_\infty u_\infty^2)$, and p_∞, ρ_∞, and u_∞ are the pressure, density, and velocity of incoming flow, respectively) on the bottom surface of the cavity calculated based on three sets of meshes and the test results (Plentovich et al., 1993). The pressure data are measured on a line probe with a lateral distance of 60.96 mm from the central line of the cavity. At the front and mid parts of the cavity, the simulation results are in good agreement with the test results, and the pressure coefficient exhibits a trend of uniform distribution close to 0. At the rear part of the cavity bottom surface, the pressure value increases rapidly with the increase of d/D_1 (d is the distance from the point probe to the front wall of cavity). The

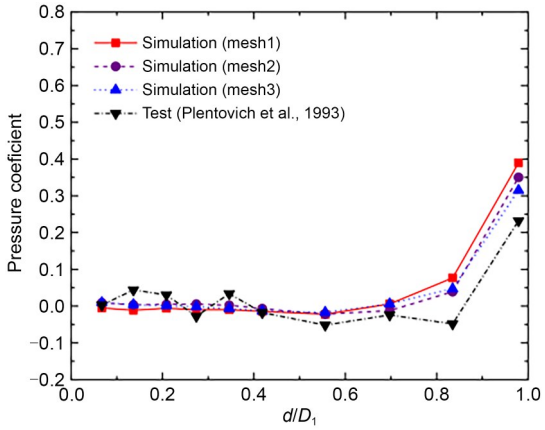

Fig. 6 Comparison of simulation and test results of the pressure distribution

simulation results indicate an overestimation of the pressure values but still align with the observed trend of the test results. With the further refinement of the mesh, this situation does not significantly improve. Therefore, the difference in the pressure results at the rear part of the cavity is likely to be caused by the difference between the simulation and the actual test environment, including differences in inflow quality and failure to fully reproduce the geometry of facilities in the wind tunnel test (the cavity is installed on a suspended flat plate in the wind tunnel test). Considering that the pressure distribution at the bottom of the cavity obtained by current simulation has the same trend as the test results, and the difference between them is also within an acceptable range, it is appropriate to adopt the mesh parameters of mesh2 to generate the surface mesh of the bogie cavity.

4.2 Simple bogie case

The simple bogie model proposed by Zhu (2015) is selected as another case to validate the mesh strategy and numerical methods. The model is composed of two wheelsets and a simple side frame, and is 1∶10 scale, with the wheel diameter D_2 equal to 92.0 mm and axle diameter d_2 equal to 17.5 mm. Since the model is symmetric about the midspan section of the axle, the wind tunnel test in (Zhu, 2015) was conducted on a half-bogie model, as shown in Fig. 7a. The computational domain and boundary conditions of this case are shown in Fig. 7b, and are also consistent with the settings in (Zhu, 2015).

To test the influence of grid size, three sets of meshes are established by modifying the grid size of

the bogie surface and the volume grid size around the bogie, named as mesh1–mesh3, and the volume cell counts of them are 2.8 million, 3.9 million, and 9.0 million, respectively. The corresponding mesh parameters are listed in Table 3, and the mesh parameters of mesh2 are close to the surface grid size of the bogie in Section 3.2.

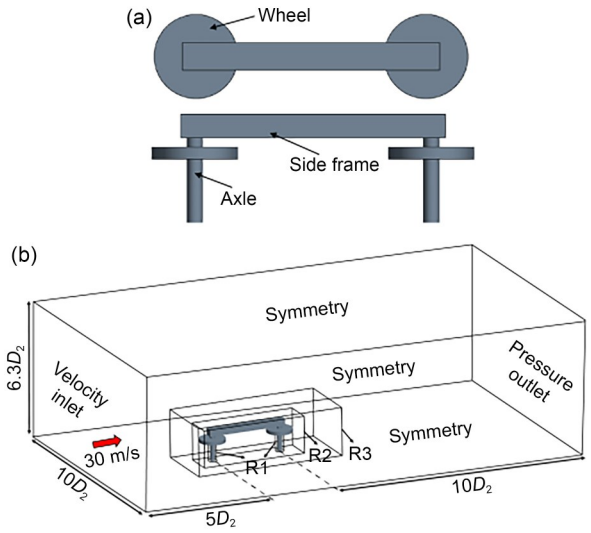

Fig. 7 Simple bogie model and corresponding computational domain: (a) half-bogie model; (b) computational domain

Table 3 Mesh parameters of the simple bogie case

Part	Grid size (mm)		
	mesh1	mesh2	mesh3
Axle	0.75	0.375	0.1875
Wheel and side frame	1.5	1.5	0.75
Region1 (R1)	0.75	0.75	0.375
Region2 (R2)	1.5	1.5	1.5
Region3 (R3)	3.0	3.0	3.0

The far-field noise results of the receiver named 'top microphone' in (Zhu, 2015) is used to validate the numerical results. The specific coordinates of the receiver can also be found in (Zhu, 2015). Fig. 8 illustrates a comparison between the spectrum results obtained by current simulation and from the wind tunnel test. The simulation results based on three sets of meshes and test results are in good agreement with regard to spectrum shape. The main frequency of the wheelset lift fluctuation is also well predicted by the three sets of meshes, with relative errors of 7.0%, 2.2%, and 2.3%, respectively. However, the sound pressure level at this frequency in the simulation results is slightly higher than the test results, and the same phenomenon was found in the numerical results in (Zhu, 2015). This is mainly because the symmetry boundary used in the simulation has stronger spanwise uniformity than the solid wall used in the experiment, which strengthens the coherent vortex shedding on the axle and makes noise level corresponding to the vortex shedding frequency higher (Zhu, 2015). Considering that the difference between the simulation results of mesh2 and mesh3 is small and the results of them are closer to the test results, it is appropriate to apply the mesh parameters of mesh2 to the aerodynamic noise simulation of the bogie region.

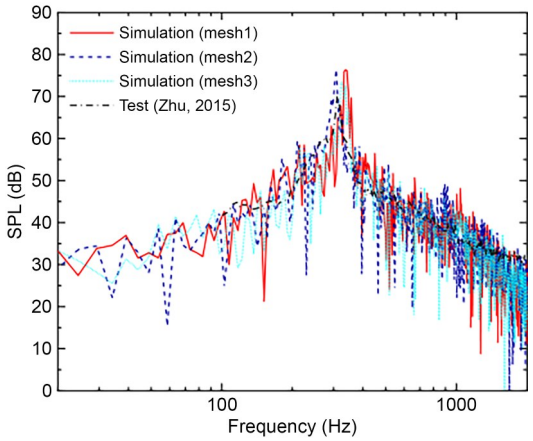

Fig. 8 Far-field noise comparison for the simple bogie model

5 Results and discussion

5.1 Flow field results

Accurate simulation of the flow field is the premise of accurate prediction of the far-field noise. In this section, the time-averaged flow field and fluctuating flow field results obtained by the four models are compared and analyzed to evaluate the effect of different modeling methods on flow field in the train head and bogie region.

5.1.1 Time-averaged pressure

The pressure distribution on the section where the carbody is truncated in the CDSM and SM is checked first (For the CSM and TCMM, the time-averaged pressure data are extracted on the section that at the same position relative to the carbody), as shown in

Fig 9. It is evident that due to the implementation of a 0-gauge pressure-outlet boundary condition in the CDSM, it fails to reproduce the pressure distribution with gradient on this section as the TCMM, CSM, and SM do. Compared with the TCMM, the CSM overestimates the negative pressure around the train, while the SM underestimates the negative pressure on both sides of the lower part of the carbody, but the relative difference between the results of SM and TCMM is not as obvious as that between CSM and TCMM. Overall, on this section, the pressure distribution of SM is the closest to that of TCMM.

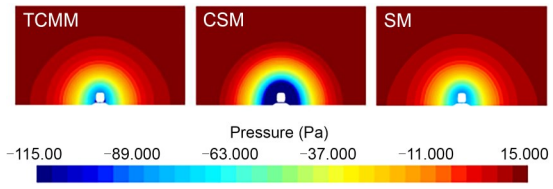

Fig. 9 Time-averaged pressure distribution on the outlet section. References to color refer to the online version of this figure

Fig. 10 further presents the time-averaged pressure distribution on the central line of the train head to provide a quantitative comparison. A local coordinate system is defined to describe the position of the pressure probe, where l is the longitudinal distance between the point probe and the nose tip of the train head, L=3.67H is the total length of the geometry model of the CDSM and SM, and the value of l/L is taken as the abscissa in Fig. 10. It can be observed that there is an excellent agreement among pressure results of all four models on the streamlined surface. Downstream from the streamlined surface, the pressure on the straight section of the carbody gradually recovers to zero. Comparatively, the CDSM exhibits a faster pressure recovery than the TCMM, while the CSM shows a slightly slower recovery. The pressure results of the SM and TCMM exhibit the closest agreement. At the lower part of the carbody, two negative pressure peaks can be observed near the front edge of the cowcatcher and the rear edge of the bogie cavity, which indicate the strong flow separation there. For the negative pressure peak at the bottom of the cowcatcher, the TCMM and CSM yield relatively consistent results, which are higher than those obtained from the CDSM and SM. At the rear edge of the bogie cavity, all three simplified models slightly underestimate the negative pressure compared to

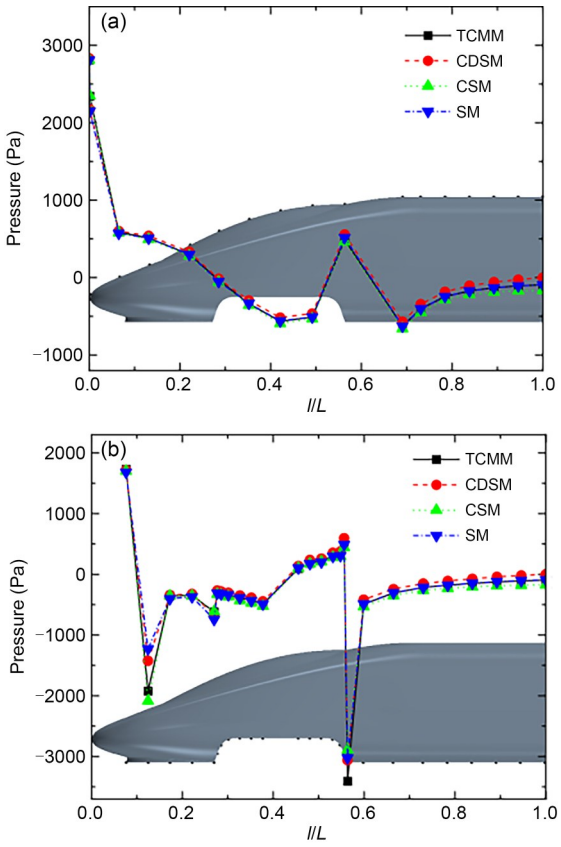

Fig. 10 Time-averaged pressure distribution on the central line of the train head: (a) upper part of train head; (b) lower part of train head

TCMM. Downstream from the cavity, similar trends of pressure recovery to that of the upper part can be observed.

5.1.2 Time-averaged velocity

Fig. 11 illustrates the time-averaged velocity distribution on longitudinal section S1 and horizontal section S2. The results show that the time-averaged velocity field results of the four models are also in good agreement; even the vortex patterns in the bogie cavity are not significantly different. When the airflow passes the front side edge of the bogie cavity, a shear layer forms and extends downstream. The airflow diverted downward from the nose tip forms a small separation zone at the front edge of the cowcatcher, which corresponds to the first negative pressure peak observed in Fig. 10b. Then, the airflow reattaches to the bottom surface of the cowcatcher and forms a jet shear layer when passing the rear edge of the cowcatcher, resulting in a clear boundary with the low-speed zone in the cavity.

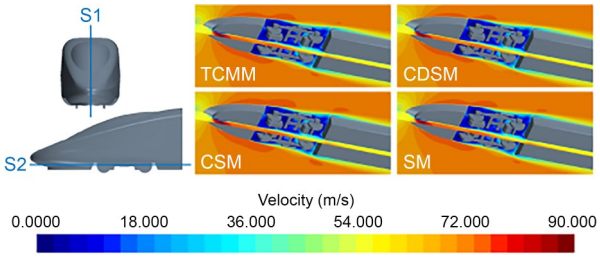

Fig. 11 Time-averaged velocity distribution. References to color refer to the online version of this figure

Fig. 12 provides a quantitative comparison of the time-averaged velocity distribution in the shear layers below and on the side of the bogie cavity. Two line probes are located on sections S1 and S2, as marked in the background of Fig. 12. Below the bogie cavity, the streamwise velocity V_x experiences a rapid decrease after entering the bogie cavity area. At the rear edge of the cavity, a peak of V_x can be observed due to the local flow acceleration caused by the diversion effect of the cavity rear wall. After the airflow leaves the cavity area, V_x gradually increases. The time-averaged lateral velocity V_y is not equal to 0, which is attributed to the asymmetry of the bogie structures. The vertical velocity component V_z initially increases to the maximum positive value after the airflow enters the bogie cavity area, which corresponds to the process of the shear layer rolling up to enter the cavity. The consistency of the maximum value and change tendency of V_z in the four models indicates that they predict identical positions where the shear layer rolls up. After that, V_z quickly changes to the maximum negative value, which corresponds to part of the airflow flowing out of the bogie cavity due to the obstruction of the cavity rear wall. On the side of the cavity, the distribution of streamwise velocity V_x resembles to that observed at the line probe beneath the cavity, because only in terms of flow in x-direction, the flow at these two positions can be perceived as airflow passing through a backward step and a forward step in tandem. In the middle part of the line probe, a significant difference can be observed between the V_x results of CDSM, SM, and TCMM, while the difference between the results of CSM and TCMM is minor. The lateral velocity V_y shows a small negative value first, indicating that the airflow tends to roll inward to enter the cavity from both sides. At the rear edge of the cavity, V_y becomes negative again, which is due to the cavity rear wall forcing the airflow to turn to both sides. The distribution of the vertical velocity V_z is similar to that observed at the line probe beneath the cavity, indicating

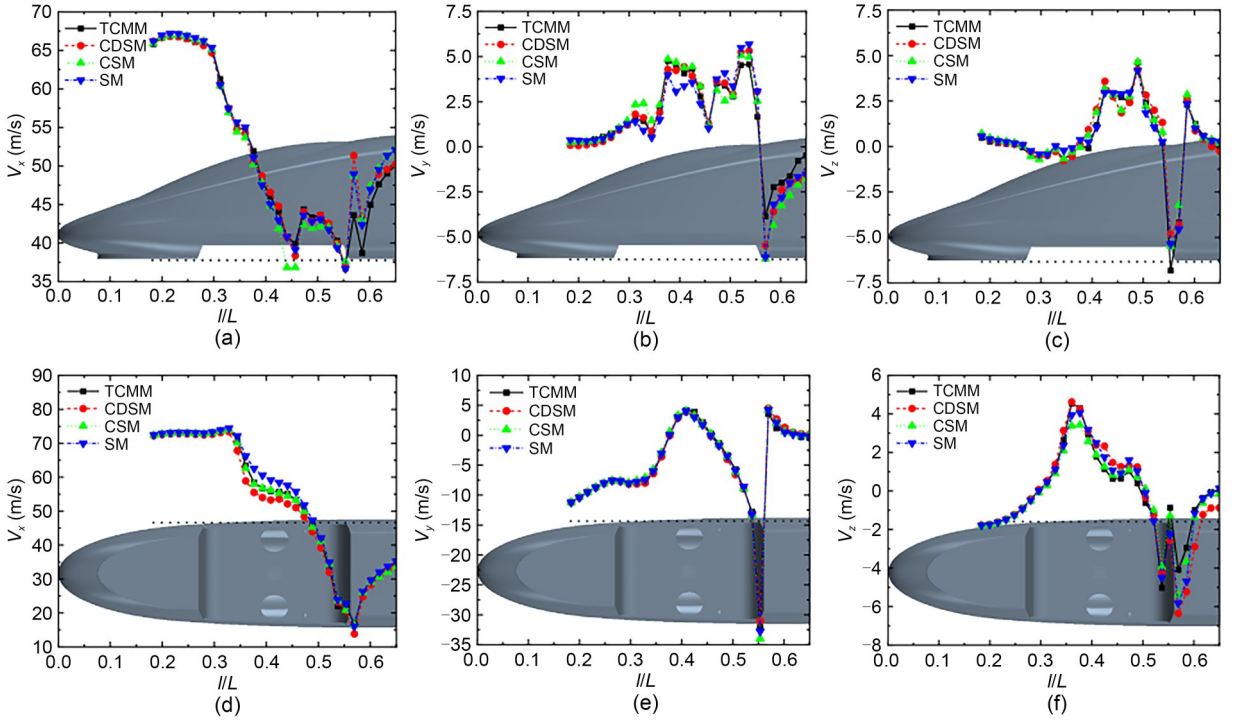

Fig. 12 Time-averaged velocity distribution in the shear layers below (a, b, and c) and on the side (d, e, and f) of the bogie cavity: (a and d) V_x; (b and e) V_y; (c and f) V_z

that the velocity field here is also affected by the shear layer rolling up below the cavity.

5.1.3 Fluctuating pressure

Fig. 13 shows the fluctuating pressure distribution of the train head and bogie region of the four models. Obviously, the amplitude of the fluctuating pressure in the lower part of the train is much higher than that in the upper part. The most violent pressure fluctuation occurs at the bottom of the cowcatcher, the lower surface of the bogie, the rear wall of the bogie cavity, and the carbody surface connected to the cavity rear wall. These locations are also the areas with the highest dipole source intensity.

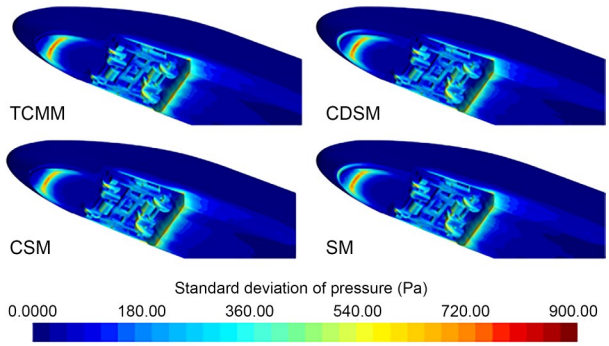

Fig. 13 Fluctuating pressure distribution in the train head and bogie region. References to color refer to the online version of this figure

Fig. 14 further compares the fluctuating pressure results on the central line of the train head. On the head streamlined surface, significant relative differences can be observed between the simulation results of the four models. Among them, the results of CDSM and SM are relatively consistent, while the results of CSM and TCMM are closer. Compared with TCMM and CSM, the CDSM and SM underestimate the intensity of the pressure fluctuation on the head streamlined surface, and with the increase of l/L, this kind of underestimation becomes more obvious. Considering the differences between the four models, this underestimation is likely due to the use of non-time-varying outlet boundary conditions in CDSM and SM. At the lower part of the carbody, the simulation results of the four models have the same trend, and the relative difference is small. Two fluctuating pressure peaks appear at the front of the bottom surface of the cowcatcher and the lower part of the cavity rear wall, which are

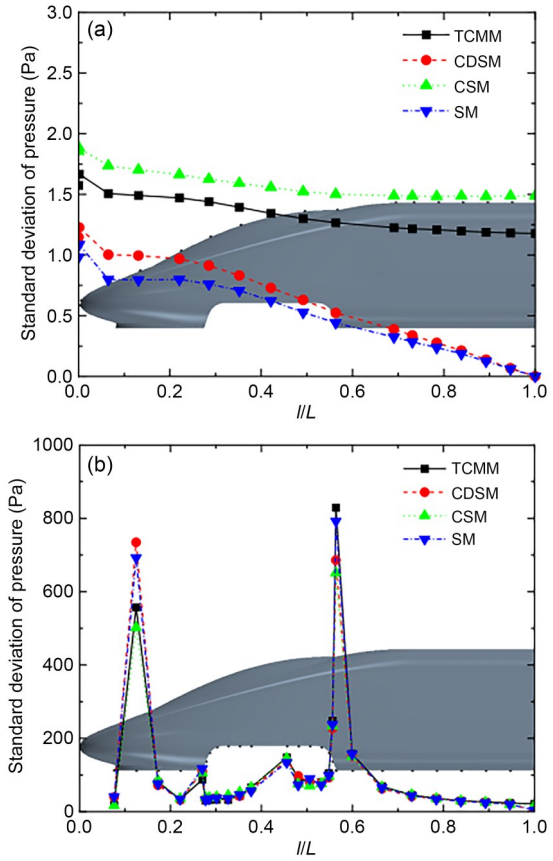

Fig. 14 Fluctuating pressure distribution on the central line of the train head: (a) upper part of train head; (b) lower part of train head

consistent with the two negative pressure peaks observed in Fig. 10b. The largest relative difference between the four models also occurs in these two positions. At the bottom surface of the cowcatcher, the simulation results of the CSM and TCMM are relatively consistent, while the CDSM and SM underestimate the amplitude of the fluctuating pressure here. At the rear edge of the bogie cavity, the results of the SM and TCMM are relatively consistent, while the CDSM and CSM underestimate the amplitude of the fluctuating pressure here.

5.1.4 Fluctuating velocity

Fig. 15 shows the time-averaged turbulent kinetic energy $\overline{E_{\mathrm{TK}}}$ distribution on sections S1 and S2 ($E_{\mathrm{TK}}=(u_i'u_i')/2$; u_i' is the fluctuating velocity in the x_i direction). Obviously, the most intense velocity fluctuation also occurs in the bogie region, especially in the shear layers formed at the rear edge of the cowcatcher and the front side edge of the bogie cavity.

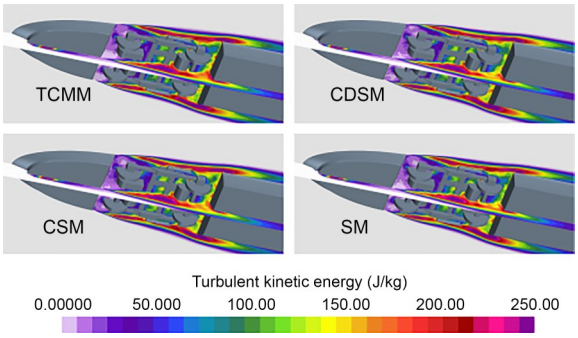

Fig. 15 Time-averaged turbulent kinetic energy distribution. References to color refer to the online version of this figure

Fig. 16 presents a quantitative comparison of the fluctuating velocity in the shear layers below and on the side of the bogie cavity. The results show that the fluctuating velocity profile in the shear layers below and on the side of the bogie cavity simulated by the four models has good consistency and the relative difference between the results of the four models presents a random distribution. As the strength of the velocity fluctuation can reflect the stability of the shear layer, the above results also indicate that the dynamic processes of formation, development, and destabilization of the shear layers in the four models are also quite consistent.

5.1.5 Vortex structures

Fig. 17 shows the instantaneous vortex structures defined by the Q-criterion (the carbody surface is colored by instantaneous pressure fluctuation). Q is the second invariant of the velocity gradient tensor, defined as $Q=\frac{1}{2}\left(\Omega_{ij}\Omega_{ij}-S_{ij}S_{ij}\right)$, where Ω_{ij} is the element of vorticity tensor, and S_{ij} is the element of rate-of-strain tensor. As is evident from the observations, there is a remarkable consistency in the instantaneous vortex structures across the four models. At the front part of the cowcatcher, the vortex structures formed by the flow separation interact with the bottom surface of the cowcatcher, causing severe pressure fluctuations there. The shear vortex structures with high vorticity form at the leading edge of the bogie cavity, develop downstream, and then roll up and invade into the cavity, resulting in a strong impingement on the lower part of the bogie and the rear wall of the bogie cavity, as well as violent pressure fluctuation there.

5.2 Far-field noise results

As shown in Fig. 18, the receivers for far-field noise assessment are arranged along two circles (a horizontal circle in the *XOY* plane and a vertical one in the *YOZ*

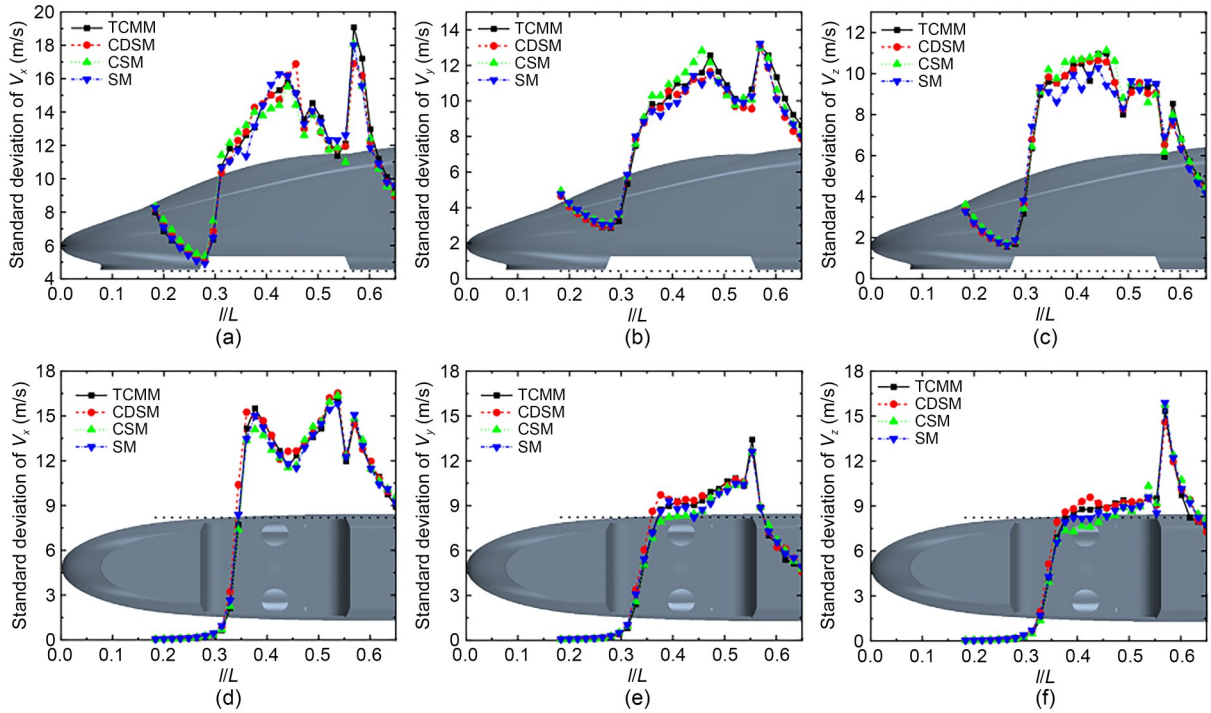

Fig. 16 Fluctuating velocity distribution in the shear layers below (a, b, and c) and on the side (d, e, and f) of the bogie cavity: (a and d) standard deviation of V_x; (b and e) standard deviation of V_y; (c and f) standard deviation of V_z

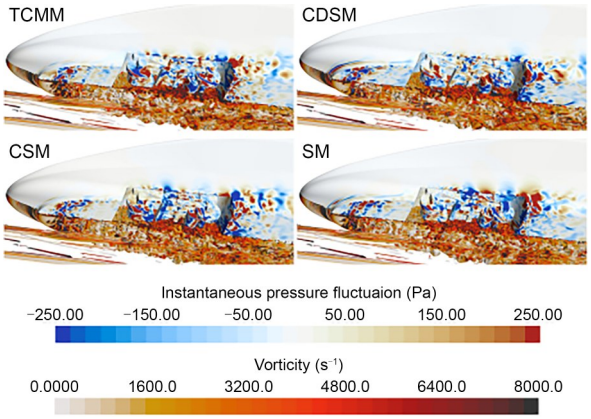

Fig. 17 Instantaneous vortex structures defined by *Q*-criterion (*Q*=5000). References to color refer to the online version of this figure

plane); the centers of the circles coincide with the geometry center of the bogie model and the radius is 2.5 m.

As mentioned earlier, the train head (Fig. 1b) and bogie region (Fig. 1c) are used as source surfaces to calculate the far-field noise. Fig. 19 presents the comparison of the overall sound pressure level (OASPL) results of the four models. In most radiation directions, there is no obvious difference between the OASPL results of the two source configurations, indicating that the noise radiation of the train head in most directions is dominated by the bogie region. The most significant difference between the results of the two source configurations occurs within a small radiation-angle range on both sides of the bogie, with a maximum difference of about 3 dB. In addition, at the receiver above the bogie in the *YOZ* plane, the OASPL results with the train head used as the source are slightly higher than those when the bogie region is used as the source, with a difference of about 1.5 dB. Based on the definition of the source surfaces, the aforementioned differences can be attributed to the contribution of dipole sources distributed on the head streamlined surface and cowcatcher. Considering that these dipole sources can make significant contribution to the far-field noise in some specific directions, it is more rational to use the entire train head (encompassing the head streamlined surface, cowcatcher, and bogie region) as the noise source when conducting aeroacoustics optimization for the bogie region.

To give a quantitative description of the difference in the far-field noise results between the three simplified models and the TCMM, define ΔSPL as the absolute value of the difference between the OASPL results of the simplified model and TCMM. Based on the OASPL results in Fig. 19, the average and maximum ΔSPL of the three simplified models are summarized in Fig. 20. The results show that when the bogie region is set as the source surface, the differences between the far-field noise results of the three simplified models and that of the TCMM are all within 1 dB. This is consistent with the comparison of the fluctuating pressure results at the lower part of the carbody shown in Fig. 14b. When the train head is set as the source surface, the maximum difference between the OASPL results of the CDSM and TCMM is around 1.8 dB, and the maximum difference between the OASPL results of the SM and TCMM is around 1.3 dB, both occurring at p*xy*28 (marked in Fig. 18); while the difference between the OASPL results of the CSM and TCMM here is still less than 1 dB. According to the previous analysis, the dipole sources on the head streamlined surface and cowcatcher make a significant contribution to the total noise at this receiver. Combined

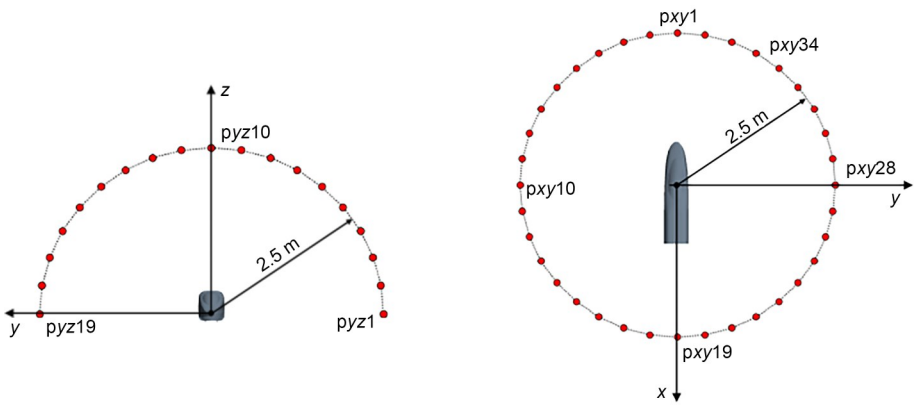

Fig. 18 Arrangement of the far-field noise receivers

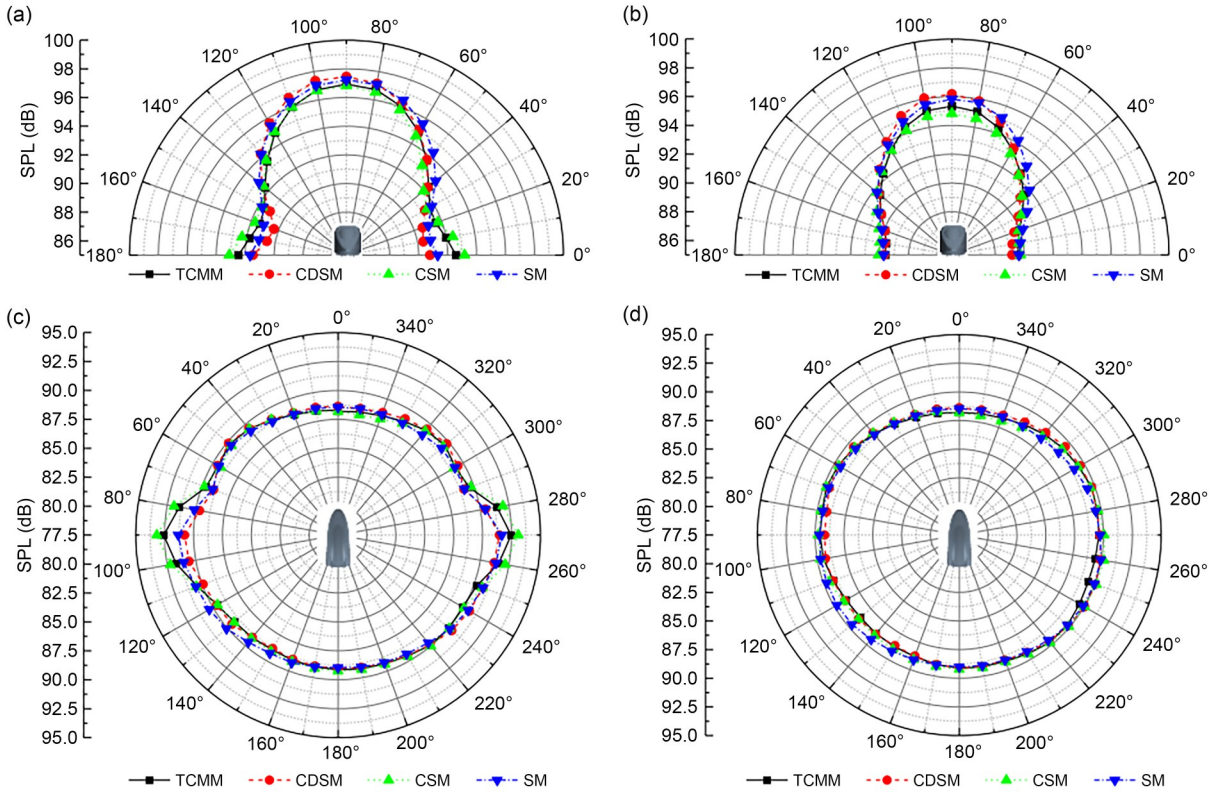

Fig. 19 OASPL results in the *XOY* and *YOZ* planes: (a) train head, *YOZ* plane; (b) bogie region, *YOZ* plane; (c) train head, *XOY* plane; (d) bogie region, *XOY* plane

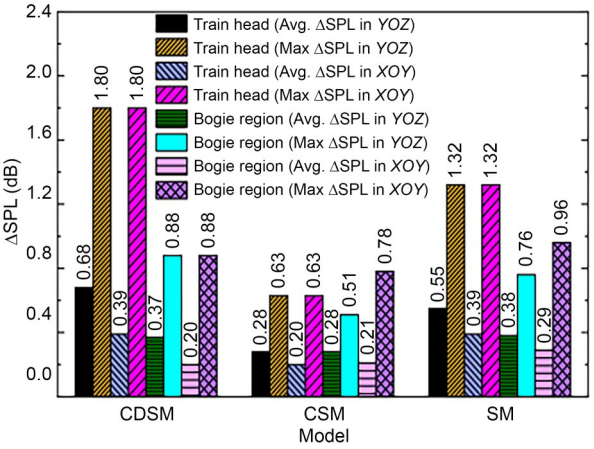

Fig. 20 Statistics of the difference between the OASPL results of the three simplified models and TCMM

with the fluctuating pressure results in the upper part of the train shown in Fig. 14a, the difference between the OASPL results of the CDSM, SM, and TCMM at this receiver can be attributed to underestimation of the pressure fluctuation on head streamlined surface in the CDSM and SM. In addition, in terms of the average difference, the results of the CSM and TCMM also have minimal discrepancy, regardless of whether the bogie region or the train head is used as the source surface.

Fig. 21 further shows the sound pressure level (SPL) spectrum results at p*xy*34 and p*xy*28. At p*xy*34, whether the train head or bogie region is used as the source surface, the spectrum results of the four models show little difference in the frequency band above 100 Hz. This is because the dipole sources on the streamlined surface and cowcatcher make no obvious contribution to the total noise there. In the frequency band below 100 Hz, the difference in sound pressure level is mainly due to the fact that the current sampling time is not long enough to analyze the low-frequency noise components (below 100 Hz). At p*xy*28, when the bogie region is set as the source surface, the spectrum results of the four models are also in good agreement above 100 Hz. However, when the train head is considered as the source surface, the SPLs of the TCMM and CSM in the frequency band with a central frequency of 630 Hz are about 10 dB higher than those of the CDSM and SM, which accounts for the difference in OASPL results at p*xy*28 observed in Fig. 19.

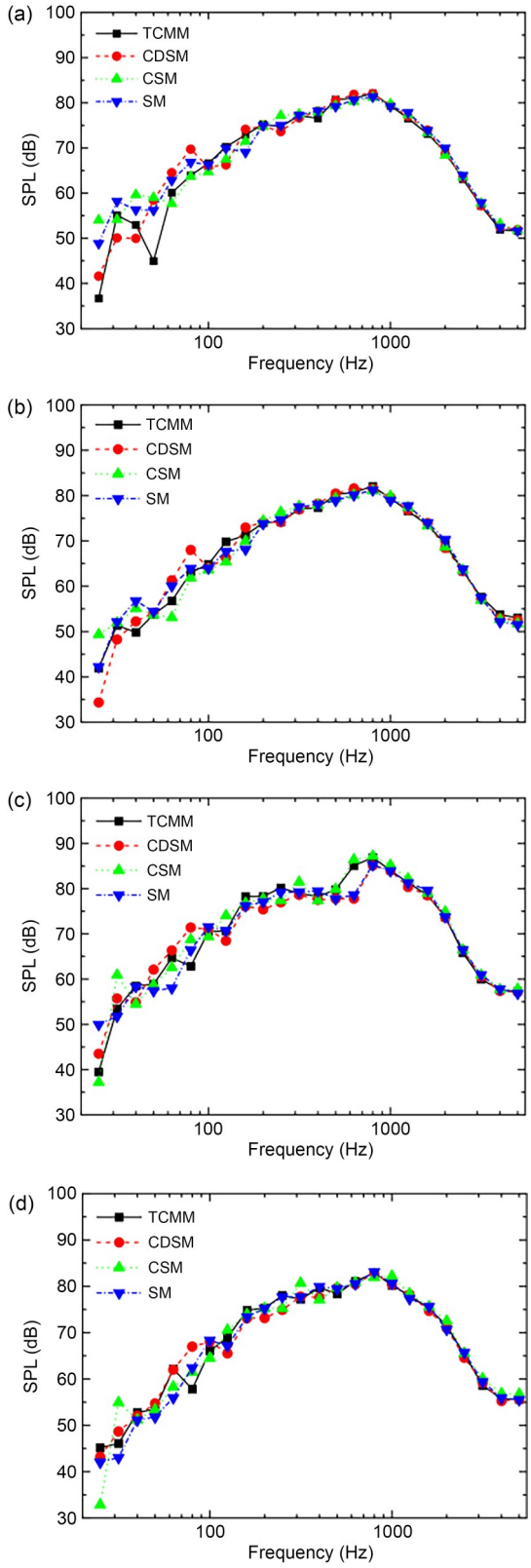

Fig. 21 Noise spectrum results of p*xz*34 and p*xz*28: (a) p*xy*34 (train head); (b) p*xy*34 (bogie region); (c) p*xy*28 (train head); (d) p*xy*28 (bogie region)

6 Conclusions

In order to determine a suitable modeling method to make CFD-based aeroacoustics optimization more efficient for the bogie region of high-speed trains. A numerical study is conducted to evaluate the effect of different modeling methods on flow field and aerodynamic noise in the foremost bogie region of a high-speed train in this paper. The reliability of the numerical methods is indirectly validated through a clean cavity case and simple bogie case. By comparing and analyzing the simulation results, the following conclusions are drawn:

(1) The time-averaged pressure distributions on the train surface predicted by the three simplified models are in good agreement with the results of the TCMM. The slight difference in pressure distribution caused by model simplification is only observed in the straight section of the carbody downstream from the head streamlined surface. The time-averaged velocity fields in the bogie region predicted by the three simplified models are also consistent with the results of the TCMM.

(2) The pressure fluctuation at the lower part of the train is much more intense than that at the upper part of the train. Compared with the TCMM, pressure fluctuation results in the bogie region of all the three simplified models are in consistent with those of the TCMM. As for the upper part of the train, both the CDSM and SM show an underestimation of the pressure fluctuation here, while the result of the CSM is in good agreement with that of the TCMM. The usage of the non-time-varying outlet boundary conditions in the CDSM and SM is likely to weaken the pressure fluctuation on the head streamlined surface and the carbody surface upstream the outlet boundary.

(3) The most severe velocity fluctuation also occurs in the bogie region, especially in the shear layers formed at the front side edge of the bogie cavity and the rear edge of the cowcatcher. The fluctuating velocity results of all four models are also in good agreement. Since the strength of the velocity fluctuation can reflect the stability of the shear layer, it can be considered that the dynamic processes of the formation, development, and destabilization of the shear layers in the four models also appear to be consistent.

(4) When only the bogie region is used as the noise source, the far-field noise results of the three

simplified models are very consistent with those of the TCMM, with difference of OASPL within 1dB. When the whole train head is used as the source surface, due to the underestimation of dipole source intensity on head streamlined surface in the CDSM and SM, the OASPL results of them and of the TCMM can differ by up to 1.3 dB and 1.8 dB in certain specific directions, while the difference between the OASPL results of the CSM and TCMM is still less than 1 dB. Therefore, the CSM seems to be a good choice for aeroacoustics optimization of the bogie region. It can significantly improve the efficiency of CFD simulation while ensuring consistency with the results of the TCMM.

Acknowledgments

This work is supported by the National Natural Science Foundation of China (No. 12172308) and the National Key Research and Development Program of China (No. 2020YFA0710902).

Author contributions

Jiawei SHI and Yuan HE designed the research. Jiawei SHI processed the corresponding data and wrote the first draft of the manuscript. Jiye ZHANG and Tian LI revised and edited the final version.

Conflict of interest

Jiawei SHI, Yuan HE, Jiye ZHANG, and Tian LI declare that they have no conflict of interest.

References

Bell JR, Burton D, Thompson MC, et al., 2017. A wind-tunnel methodology for assessing the slipstream of high-speed trains. *Journal of Wind Engineering and Industrial Aerodynamics*, 166:1-19. https://doi.org/10.1016/j.jweia.2017.03.012

Chang C, Li T, Qin D, et al., 2022. On the scale size of the aerodynamic characteristics of a high-speed train. *Journal of Applied Fluid Mechanics*, 15(1):209-219. https://doi.org/10.47176/jafm.15.01.33041

Ding SS, Li Q, Tian AQ, et al., 2016. Aerodynamic design on high-speed trains. *Acta Mechanica Sinica*, 32(2):215-232. https://doi.org/10.1007/s10409-015-0546-y

Dong TY, Liang XF, Krajnović S, et al., 2019. Effects of simplifying train bogies on surrounding flow and aerodynamic forces. *Journal of Wind Engineering and Industrial Aerodynamics*, 191:170-182. https://doi.org/10.1016/j.jweia.2019.06.006

Farassat F, 2007. Derivation of Formulations 1 and 1A of Farassat. Technical Report No. NASA/TM-2007-214853, NASA Langley Research Center, Hampton, USA.

Gao Y, Li QL, Wang YG, 2017. Analysis method of aerodynamic noise of full scale high speed train head shape. *Journal of Dalian Jiaotong University*, 38(3):30-35 (in Chinese). https://doi.org/10.13291/j.cnki.djdxac.2017.03.007

Guo ZJ, Liu TH, Chen ZW, et al., 2020. Aerodynamic influences of bogie's geometric complexity on high-speed trains under crosswind. *Journal of Wind Engineering and Industrial Aerodynamics*, 196:104053. https://doi.org/10.1016/j.jweia.2019.104053

Karbon KJ, Dietschi UD, 2005. Computational analysis and design to minimize vehicle roof rack wind noise. *Journal of Passenger Car: Mechanical Systems Journal*, 114(6): 649-656.

Khier W, Breuer M, Durst F, 2000. Flow structure around trains under side wind conditions: a numerical study. *Computers & Fluids*, 29(2):179-195. https://doi.org/10.1016/S0045-7930(99)00008-0

Kim H, Hu ZW, Thompson D, 2020. Numerical investigation of the effect of cavity flow on high speed train pantograph aerodynamic noise. *Journal of Wind Engineering and Industrial Aerodynamics*, 201:104159. https://doi.org/10.1016/j.jweia.2020.104159

Lauterbach A, Ehrenfried K, Loose S, et al., 2012. Microphone array wind tunnel measurements of Reynolds number effects in high-speed train aeroacoustics. *International Journal of Aeroacoustics*, 11(3-4):411-446. https://doi.org/10.1260/1475-472X.11.3-4.411

Li T, Dai ZY, Zhang WH, 2020a. Effect of RANS model on the aerodynamic characteristics of a train in crosswinds using DDES. *Computer Modeling in Engineering & Sciences*, 122(2):555-570. https://doi.org/10.32604/cmes.2020.08101

Li T, Qin D, Zhang WH, et al., 2020b. Study on the aerodynamic noise characteristics of high-speed pantographs with different strip spacings. *Journal of Wind Engineering and Industrial Aerodynamics*, 202:104191. https://doi.org/10.1016/j.jweia.2020.104191

Li ZM, Li QL, Yang ZG, 2022. Flow structure and far-field noise of high-speed train under ballast track. *Journal of Wind Engineering and Industrial Aerodynamics*, 220: 104858. https://doi.org/10.1016/j.jweia.2021.104858

Liu JL, Zhang JY, Zhang WH, 2011. Numerical analysis on aerodynamic noise of the high-speed train head. *Journal of the China Railway Society*, 33(9):19-26 (in Chinese). https://doi.org/10.3969/j.issn.1001-8360.2011.09.003

Meskine M, Pérot F, Kim MS, et al., 2013. Community noise prediction of digital high speed train using LBM. The 19th AIAA/CEAS Aeroacoustics Conference. https://doi.org/10.2514/6.2013-2015

Minelli G, Yao HD, Andersson N, et al., 2020. An aeroacoustic study of the flow surrounding the front of a simplified ICE3 high-speed train model. *Applied Acoustics*, 160:107125. https://doi.org/10.1016/j.apacoust.2019.107125

Plentovich EB, Stallings Jr RL, Tracy MB, 1993. Experimental Cavity Pressure Measurements at Subsonic and Transonic Speeds. Technical Report No. NASA-TP-3358, NASA Langley Research Center, Hampton, USA.

Schell A, Eiselt M, 2020. Numerical investigation of tonal noise at automotive side mirrors due to aeroacoustic feedback.

The 11th International Styrian Noise, Vibration & Harshness Congress: the European Automotive Noise Conference. https://doi.org/10.4271/2020-01-1514

Shi JW, Zhang JY, 2024. Effect of bogie cavity end wall inclination on flow field and aerodynamic noise in the bogie region of high-speed trains. *CMES-Computer Modeling in Engineering & Sciences*, 139(2):2175-2195. https://doi.org/10.32604/cmes.2023.043539

Shi JW, Zhang JY, Li T, 2024. Aerodynamic noise reduction of high-speed pantograph by introducing planar jet on leeward surface of panhead. *Journal of Wind Engineering and Industrial Aerodynamics*, 250:105780. https://doi.org/10.1016/j.jweia.2024.105780

Shur ML, Spalart PR, Strelets MK, et al., 2008. A hybrid RANS-LES approach with delayed-DES and wall-modelled LES capabilities. *International Journal of Heat and Fluid Flow*, 29(6):1638-1649. https://doi.org/10.1016/j.ijheatfluidflow.2008.07.001

Siemens PLM software, 2017. STAR-CCM+User Guide (Version 12.04). Siemens.

Spalart PR, Deck S, Shur ML, et al., 2006. A new version of detached-eddy simulation, resistant to ambiguous grid densities. *Theoretical and Computational Fluid Dynamics*, 20(3):181-195. https://doi.org/10.1007/s00162-006-0015-0

Thompson DJ, 2008. Railway Noise and Vibration: Mechanisms, Modelling and Means of Control. Elsevier, Amsterdam, the Netherlands.

Thompson DJ, Iglesias EL, Liu XW, et al., 2015. Recent developments in the prediction and control of aerodynamic noise from high-speed trains. *International Journal of Rail Transportation*, 3(3):119-150. https://doi.org/10.1080/23248378.2015.1052996

Wang JB, Minelli G, Dong TY, et al., 2020. Impact of the bogies and cavities on the aerodynamic behaviour of a high-speed train. An IDDES study. *Journal of Wind Engineering and Industrial Aerodynamics*, 207:104406. https://doi.org/10.1016/j.jweia.2020.104406

Williams JEF, Hawkings DL, 1969. Sound generation by turbulence and surfaces in arbitrary motion. *Philosophical Transactions of the Royal Society A: Mathematical, Physical and Engineering Sciences*, 264(1151):341-342.

Yao HD, Chroneer Z, Davidson L, 2018. Simplifications applied to simulation of turbulence induced by a side view mirror of a full-scale truck using DES. WCX World Congress Experience. https://doi.org/10.4271/2018-01-0708

Zhao YY, Yang ZG, Li QL, et al., 2020. Analysis of the near-field and far-field sound pressure generated by high-speed trains pantograph system. *Applied Acoustics*, 169: 107506. https://doi.org/10.1016/j.apacoust.2020.107506

Zhu JY, 2015. Aerodynamic Noise of High-Speed Train Bogies. PhD Thesis, University of Southampton, Southampton, UK.

Zhu JY, Hu ZW, 2017. Flow between the train underbody and trackbed around the bogie area and its impact on ballast flight. *Journal of Wind Engineering and Industrial Aerodynamics*, 166:20-28. https://doi.org/10.1016/j.jweia.2017.03.009